Title

Retinal Structure and Gene Therapy Outcome in Retinoschisin-Deficient Mice Assessed by Spectral-Domain Optical Coherence TomographyOCT Imaging of Retinoschisin Knockout Mouse

Journal

Investigative Ophthalmology & Visual Science, 57(9)

ISSN

0146-0404

Authors

Zeng, Yong
Petralia, Ronald S
Vijayasarathy, Camasamudram
et al.

Publication Date

2016-07-13

DOI

10.1167/iovs.15-18920

Peer reviewed

Special Issue

Retinal Structure and Gene Therapy Outcome in Retinoschisin-Deficient Mice Assessed by Spectral-Domain Optical Coherence Tomography

Yong Zeng,[1] Ronald S. Petralia,[2] Camasamudram Vijayasarathy,[1] Zhijian Wu,[3] Suja Hiriyanna,[3] Hongman Song,[1] Ya-Xian Wang,[2] Paul A. Sieving,[1,4] and Ronald A. Bush[1]

[1]Section on Translational Research for Retinal and Macular Degeneration, National Institute on Deafness and Other Communication Disorders, National Institutes of Health, Bethesda, Maryland, United States
[2]Advanced Imaging Core, National Institute on Deafness and Other Communication Disorders, National Institutes of Health, Bethesda, Maryland, United States
[3]Ocular Gene Therapy Core, National Eye Institute, National Institutes of Health, Bethesda, Maryland, United States
[4]National Eye Institute, National Institutes of Health, Bethesda, Maryland, United States

Correspondence: Ronald A. Bush, National Institute on Deafness and Other Communication Disorders, National Institutes of Health, 50 South Drive, Room 4339, MSC#8021, Bethesda, MD 20892-8021, USA; bushr@nidcd.nih.gov.

Submitted: December 14, 2015
Accepted: March 20, 2016

Citation: Zeng Y, Petralia RS, Vijayasarathy C, et al. Retinal structure and gene therapy outcome in retinoschisin-deficient mice assessed by spectral-domain optical coherence tomography. *Invest Ophthalmol Vis Sci*. 2016;57:OCT277–OCT287. DOI:10.1167/iovs.15-18920

Purpose. Spectral-domain optical coherence tomography (SD-OCT) was used to characterize the retinal phenotype, natural history, and treatment responses in a mouse model of X-linked retinoschisis (*Rs1*-KO) and to identify new structural markers of AAV8-mediated gene therapy outcome.

Methods. Optical coherence tomography scans were performed on wild-type and *Rs1*-KO mouse retinas between 1 and 12 months of age and on *Rs1*-KO mice after intravitreal injection of AAV8-scRS/IRBPhRS (AAV8-*RS1*). Cavities and photoreceptor outer nuclear layer (ONL) thickness were measured, and outer retina reflective band (ORRB) morphology was examined with age and after AAV8-*RS1* treatment. Outer retina reflective band morphology was compared to immunohistochemical staining of the outer limiting membrane (OLM) and photoreceptor inner segment (IS) mitochondria and to electron microscopy (EM) images of IS.

Results. Retinal cavity size in *Rs1*-KO mice increased between 1 and 4 months and decreased thereafter, while ONL thickness declined steadily, comparable to previous histologic studies. Wild-type retina had four ORRBs. In *Rs1*-KO, ORRB1was fragmented from 1 month, but was normal after 8 months; ORRB2 and ORRB3 were merged at all ages. Outer retina reflective band morphology returned to normal after AAV-*RS1* therapy, paralleling the recovery of the OLM and IS mitochondria as indicated by anti–β-catenin and anti-COX4 labeling, respectively, and EM.

Conclusions. Spectral-domain OCT is a sensitive, noninvasive tool to monitor subtle changes in retinal morphology, disease progression, and effects of therapies in mouse models. The ORRBs may be useful to assess the outcome of gene therapy in the treatment of X-linked retinoschisis patients.

Keywords: optical coherence tomography, X-linked retinoschisis, outer nuclear layer, outer retina reflective band, AAV gene therapy

X-linked retinoschisis (XLRS) is a bilateral, recessively inherited, vitreoretinal dystrophy characterized by microcystic change in the macula and splitting throughout most retinal layers.[1] The estimated prevalence of XLRS ranges from 1:5000 to 1:25,000,[2] and it is one of the most common causes of macular degeneration in young males.[1] The histopathology of postmortem XLRS retinal tissue shows multiple retinal layers being affected, including the inner nuclear layer (INL) and the inner and outer plexiform layers (IPL and OPL).[3] These observations were also confirmed clinically with optical coherence tomography (OCT).[4] Retinoschisin (RS1) is generally believed to function as a retinal cell adhesion protein and loss of RS1 function is the underlying cause of XLRS.[5–7] To date, there are no effective treatments available for this disease.

Animal models that mimic clinical features of human disease are widely used to better understand its pathophysiology and natural progression. Models have also enabled researchers to investigate the safety and efficacy of drug candidates while seeking ways to treat human diseases.[5,8–12] To gain insights into the mechanisms of XLRS and develop a potential treatment, retinoschisin-null (*Rs1*-KO) mouse models have been established by knocking out the *Rs1* gene, the murine orthologue of human *RS1*.[7,8] The structural and functional changes observed in *Rs1*-KO mimic the clinical features of XLRS-affected males, and we previously have described the natural history of the major inner and outer retinal structural changes of *Rs1*-KO mice by using conventional histology.[13] Three independent groups have developed clinically translatable *RS1* gene therapy candidates and demonstrated structural and functional rescue

Investigative Ophthalmology & Visual Science

of the disease phenotype by augmentation of the human RS1 protein in diseased retina by using AAV-mediated gene delivery systems.[8,9,14–16]

The vertebrate retina is a complex organ composed of 10 histologic layers and five major neuron types. Histologic analysis of postmortem tissue has been the most common method to evaluate structural changes in the retina. Preparation of retinal sections for histology is a multistep process that includes eye enucleation, fixation, dehydration, cutting, flattening, and mounting. Each step is a potential source of significant alterations in structure and dimension of the tissue,[17] and this is particularly applicable to eyes with disease, such as in the *Rs1*-KO mouse. Furthermore, there are wide individual variations in disease phenotypes[13] and response to therapy, thus requiring a large number of animals to obtain reproducible and convincing conclusions.

Noninvasive OCT, on the other hand, provides rapid imaging of the retina in cross-section with micrometer resolution without time- and labor-intensive preparation of postmortem samples, enables multiple images for longitudinal studies,[18] and reduces the animal number needed to understand disease progression and potential treatment responses over time.[17–25] It has evolved over the past 2 decades to become a widely used diagnostic tool in medicine, especially in the field of ophthalmology.[20] Its wide application in animal research, especially in small animal models such as rodents, has been limited because of the relatively poor overall image quality in early spectral-domain OCT (SD-OCT) instruments. Rapid advances in instrumentation and enhanced imaging technology provide current SD-OCT systems with faster scanning speed, improved signal to noise ratio, and superior depth resolution, which enhance OCT capabilities for small-animal experimentation.[17] Spectral-domain OCT produces cross-sectional images of retina that allow monitoring of the dynamic changes in a living animal over time, making it possible to study detailed retinal integrity in mouse models of human diseases in vivo.[18,22–31]

In this study, we imaged *Rs1*-KO and wild-type (WT) animals at different ages and after gene therapy with AAV8-*RS1* vector. The natural history of cavity size and outer nuclear layer (ONL) morphology revealed in OCT images was comparable to conventional histology.[13] In addition, we demonstrated the power of OCT to evaluate the regional distribution of these changes and follow them longitudinally in a single animal. Optical coherence tomography also detected subtle alterations in the outer retina, represented by the outer retina reflective bands that correspond to anatomic structures we identified by immunohistochemistry and electron microscopy. These bands show distinctive changes with age and treatment that may have application in noninvasively monitoring the efficacy of a treatment for XLRS at the level of the outer retina.

Methods

Animals

This research was conducted in accordance with the ARVO Statement for the Use of Animals in Ophthalmic and Vision Research and was approved by the Animal Care and Use Committee of the National Eye Institute. *Rs1*-KO mice derived from founders originally described by Zeng et al.[8] and back-crossed for more than 20 generations onto C57BL/6 background were born and reared under 50-lux cyclic lighting (12 hour:12 hour) with food and water available ad libitum.

Intravitreal Injection

Recombinant AAV-*RS1* gene therapy vector described previously[32] was unilaterally administered into 28 *Rs1*-KO mice on postnatal day 21 to 26 by intravitreal injection; the contralateral eye remained untouched. *Rs1*-KO mice were anesthetized by intraperitoneal injection of ketamine (100 mg/kg) and xylazine (10 mg/kg), and one drop of 0.5% tetracaine topical anesthetic was applied to the cornea. One microliter of viral vector at a dose of 2.5×10^9 vector genomes per eye was injected into the vitreous body through the sclera on the nasal side of the eye approximately 1 mm posteriorly to the limbus with a 10-μL Nanofil syringe with a removable 35-gauge needle (World Precision Instruments, Inc., Sarasota, FL, USA). After injection, triple antibiotic ophthalmic ointment (neomycin, polymyxin B, and bacitracin) was applied to the eye.

Optical Coherence Tomography Image Collection and Analysis

Optical coherence tomography images were obtained with the Envisu R2200 SD-OCT ophthalmic imaging system (Bioptigen, Durham, NC, USA). Animals were anesthetized by intraperitoneal injection of ketamine (100 mg/kg) and xylazine (10 mg/kg) and placed in a custom holder. The pupils were dilated with a mixture of tropicamide and phenylephrine. Artificial tears (Alcon Laboratories, Inc., Fort Worth, TX, USA) were used throughout the procedure to maintain corneal hydration and clarity. Two linear B-scans (1000 A-scans per B-scan), each the average of 10 frames, were obtained from nasal to temporal pole through the optic nerve (ON) head. Radial volume scans consisting of 10 B-scans (1000 A-scans per B-scan) were collected at 18° angular intervals and were each an average of five frames. Rectangular volume scans with 100 B-scans (1000 A-scans per B-scan) were collected from the retinal pigment epithelium (RPE) to the posterior lens, across a 14×14-mm area centered on the ON head. This represents approximately one-third of the central retina of each mouse. To examine the peripheral retina, the angle between the probe and the mouse eye was changed, allowing most of the retina to be observed.

Cavity size, ONL thickness, and outer retina reflective band (ORRB) number and morphology were used to evaluate changes in retinal structure. The bit map image obtained from the average of 10 frames of linear B-scans from the same horizontal plane through the optic nerve was used to assess cavity size and ONL thickness with ImageJ 1.48v (http://imagej.nih.gov/ij; provided in the public domain by the National Institutes of Health, Bethesda, MD, USA). To measure cavity area, the gray scale image was converted to white and black with the "Adjust Threshold" command. Then the cavities were segmented by using the "Huang" method selected in the "threshold" window. This method of setting the threshold for segmentation was determined to produce the most accurate segmentation of cavities by comparison to the original images (Supplementary Fig. S1). The area of the temporal and nasal half of each image containing cavities was selected by using the freehand tool, and the "Analyze Particles" command was used to calculate the cavity area on each side of the ON. The sum of these two measurements was used as the cavity size for each retina. More rigorous custom algorithms for segmenting cavities have been used on OCT images in human retinal diseases, including XLRS.[33,34] We compared the results from our method to a second method of evaluating cavity size in the *Rs1*-KO mouse that did not require segmentation and used cavity width rather than area (see Supplementary Fig. S2). The correlation between the two methods was 0.94 (*R*-squared) in 96 retinas (Supplementary Fig. S3).

Investigative Ophthalmology & Visual Science

To examine cavity distribution, four cross-sectional images obtained from radial scans through the ON head from the nasal to temporal, inferior to superior, nasal-inferior to temporal-superior, and temporal-inferior to nasal-superior poles were used to obtain eight measurements from one animal. Outer nuclear layer thickness was measured at 300 and 500 μm from the ON head on each side in a nasal to temporal scan by using ImageJ, and these four values were averaged for each retina. Outer retina reflective band number and qualitative assessment of structure were used to monitor natural history changes and the response to AAV-*RS1* vector treatment.

For the natural history study, mice were evaluated for ONL thickness and cavity size at 1, 2, 4, 8, 10, and 12 months of age, with at least six eyes from WT and eight eyes from *Rs1*-KO mice per time point. Twenty-nine *Rs1*-KO mice were evaluated longitudinally at 4 to 5 and 7 to 8 months of age. Thirty-five eyes of *Rs1*-KO mice were evaluated for retinal distribution of cavities. Twenty-eight *Rs1*-KO mice were injected with AAV8-*RS1* at 22 to 26 days of age and evaluated 12 to 15 weeks later for cavity size, ONL thickness, and ORRB morphology.

Histology

Animals were euthanized at selected time points, at least six animals per time point, by CO_2 followed by cervical dislocation. For plastic sections, eyeballs were enucleated and fixed in 4% glutaraldehyde for 30 minutes, and transferred into 10% formalin for 48 to 72 hours before dehydration and embedding in rapid polymerizing methyl methacrylate. Sagittal and horizontal semithin sections were cut through the center of the left eye and right eye, respectively. For immunochemistry, animals were perfused with 4% paraformaldehyde in sodium phosphate buffer. The eyes were removed and fixed overnight in 4% paraformaldehyde and 0.5% glutaraldehyde in sodium phosphate buffer followed by processing for cryosectioning. Approximately 30 sagittal sections of the injected eye were collected beginning at the nasal margin of the retina and proceeding through and including the ON head and approximately 200 μm of the temporal retina. To obtain an accurate comparison, the third eyelid was retained as a landmark when collecting eyeballs.

Image Comparison

Sagittal and horizontal sections that were cut through the center of each eye were stained by haematoxylin and eosin using a standard protocol. Consecutive overlapping images were obtained by using a Nikon E800 fluorescence microscope (Nikon, Tokyo, Japan) and stitched together to form the entire retinal section by using Adobe Photoshop elements (Adobe Systems, Inc., San Jose, CA, USA). Four images from each quadrant per retina were collected with a Zeiss microscope (Carl Zeiss Microscopy, Jena, Germany). The images from OCT scans and histologic sections were compared by using cross-sections taken from approximately the same locations in each retina.

Immunochemistry

Retinal sections were rinsed in 0.1% Triton X-100 in PBS and preincubated with PBS containing 20% normal goat serum (Sigma, Steinheim, Germany) and 0.5% Triton X-100 at room temperature (RT) for 2 hours to block nonspecific antibody binding. For RS1 protein staining, the sections were incubated overnight at 4°C with a rabbit polyclonal antibody against the N-terminus of retinoschisin (amino acid residues 24–37) in washing buffer (0.1% Triton X-100 of PBS-T); for double-labeling experiments, the sections were incubated overnight at 4°C with a mixture of the following primary antibodies diluted in washing buffer: rabbit anti-RS1 (1:1000, customized antibody; Invitrogen, Eugene, OR, USA) and mouse anti–β-catenin (1:400; BD Transduction Laboratories, San Jose, CA, USA), or mouse anti–OxPhos Complex IV subunit I (1:300; Invitrogen), respectively. After washing with washing buffer, sections were incubated with an appropriate secondary antibody conjugated to red-fluorescent Alexa Fluor 568 dye or green-fluorescent Alexa 488 dye (Invitrogen) for 1 hour at room temperature. The nuclei were stained with 4′,6′-diamidino-2-phenylindole (DAPI; Invitrogen) in washing buffer, and sections were mounted with Fluorogel (Electron Microscopy Sciences, Hetfield, PA, USA). An LSM 700 confocal microscope with ZEN LE software (Carl Zeiss Microscopy) was used to capture and process retinal images, and image contrast enhancement was performed by using image-editing software (Photoshop CS6; Adobe Systems, Inc.).

Electron Microscopy

Immunoelectron microscopy was carried out as described previously with minor modifications.[35,36] Eyes were enucleated and fixed in 4% paraformaldehyde in PBS buffer (10 mM sodium phosphate, pH 7.5, 0.9% saline) for 3 hours, and the anterior part of the eye was removed. After four washes in PBS, the retinas were embedded in buffered 7% agarose TypeX1 (Sigma-Aldrich Corp., St. Louis, MO, USA). Agarose blocks were sectioned with a vibratome (Leica, Wetzlar, Germany) in 100-μm slices. Vibratome sections were blocked in 20% normal goat serum in PBS overnight at 4°C and subsequently incubated with anti-rabbit antibody against RS1 in PBS plus 5% goat serum for 2 days at 4°C. After washing, the sections were incubated with the biotinylated anti-rabbit IgG secondary antibody (Vector Laboratories, Inc., Burlingame, CA, USA) for 4 hours at RT. Then the sections were incubated with a complex consisting of avidin and biotinylated horseradish peroxidase (Vectastain ABC-Kit; Vector Laboratories) for 2 hours at RT in the dark. Subsequently, the sections were incubated in peroxidase substrate solution to obtain the desired staining intensity. The stained sections were then postfixed in 2.5% glutaraldehyde and 1% osmium, respectively; after dehydration, they were embedded in epon. Ultrathin sections were examined in a JEOL JEM-2100 transmission electron microscope (Tokyo, Japan).

Results

Retinal Structure of WT and *Rs1*-KO Mice

Figure 1 shows the retinal layers in OCT images and H&E-stained plastic sections of WT and *Rs1*-KO mice. Histologic images are from the same retina and at approximately the same position as the OCT images. The WT OCT image (Fig. 1A, left) exhibits an organized retinal laminar structure, including the ganglion cell layer (GCL), IPL, INL, OPL, ONL, outer limiting membrane (OLM), inner segment (IS), outer segment (OS), and RPE.[17,19,22] The outer retina reflective bands 1 to 4 seen in WT retinas were produced by structures between the ONL and the RPE; except for band 4 (RPE), the ORRBs were not visible or barely visible with H&E staining (Fig. 1A, right). Outer retina reflective band 4 is thought to be centered at the RPE cell body,[37] so the OCT images in Figure 1 were positioned by aligning this band with the darkly stained RPE in the histologic section (Fig. 1A, right). Although corresponding nuclear (ONL, INL, GCL) and plexiform (OPL, IPL) layers in OCT and histology images are adjacent to each other, alignment is not exact. The photoreceptor layer (ONL, IS, OS) in particular is narrower in

Investigative Ophthalmology & Visual Science

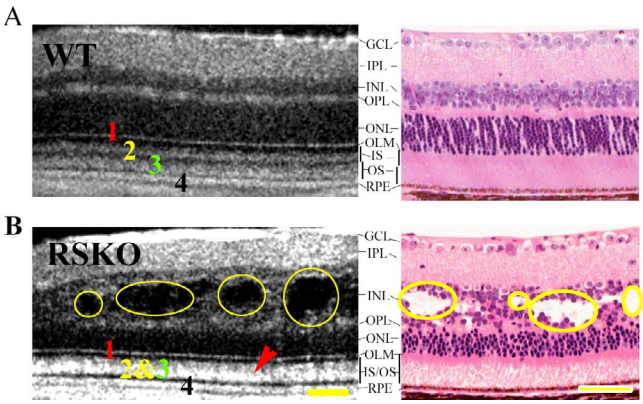

Figure 1. Comparison of retinal structure in OCT images and H&E-stained plastic sections from WT and *Rs*1-KO mice. (**A**) The major retinal layers of WT visible by histology (*right*) are in good alignment with corresponding OCT bands (*left*). There are four outer retina reflective bands clearly visible in the OCT image of WT retina distal to the ONL, labeled 1, 2, 3, and 4. These bands align with structures in the photoreceptor and RPE layer, not all of which are visible in conventional H&E-stained sections (see text). (**B**) Optical coherence tomography image and plastic section from an age-matched (4-month-old) *Rs*1-KO mouse with multiple cavities (*yellow circles*) spanning the INL and OPL, making the margins between OPL and INL and between OPL and ONL uneven and less clear. The ONL is also decreased in thickness. In addition, the second and third outer retina bands in the OCT images are replaced by a single wider reflective band (*red arrowhead*; [**B**, *left*]). *Scale bars*: 50 μm.

histologic sections, probably due to shrinkage in processing. The other ORRBs align with the OLM positioned at the outer margin of the ONL (ORRB1) and substructures within the photoreceptor inner and outer segments (ORRB2 and ORRB3 and dark bands between ORRB1 and ORRB4). Unlike the well-organized laminar structures in WT mice, the laminas in *Rs1*-KO were partially disrupted (Fig. 1B). Schisis cavities spanned the OPL and INL layers and the margins between these two layers were blurred. In addition, the ONL thickness was reduced, and the ORRBs were reduced from four to three bands (Fig. 1B, left). Cavities and reduced ONL thickness were also observed in histology sections (Fig. 1B, right). Similar to the finding in WT mouse, the ONL layer in *Rs1*-KO mouse was narrower in histologic sections than in OCT images, and in addition, cavity size appeared smaller, which may be due to shrinkage in processing.

We observed uneven distribution of the cavities within individual mice, as shown in Figures 2A and 2B. Figure 2A (top panel) shows a transverse view of the OCT rectangular volume scan at the INL level with schisis cavities exhibited as dark areas. The bottom panel shows two cross-sectional images in the same animal from a radial volume scan centered on the ON head; one displays the section from the temporal to the nasal side, and the other shows the sagittal section from superior to inferior side. These images show that cavities vary widely in distribution and size across all retinal regions, but in general, they are larger and more frequent in the superior and temporal than in the inferior and nasal quadrants. Figure 2B shows a summary of cavity distribution in 4- to 5-month-old *Rs1*-KO mice. The corresponding histology sections confirmed these differences in cavity distribution in *Rs1*-KO retinas (data not shown).

Apart from uneven distribution of the cavities within individual mice, there was a wide variation between animals in cavity size and the ONL thickness, as reported in our earlier histologic study.[13] Figure 2C shows four representative

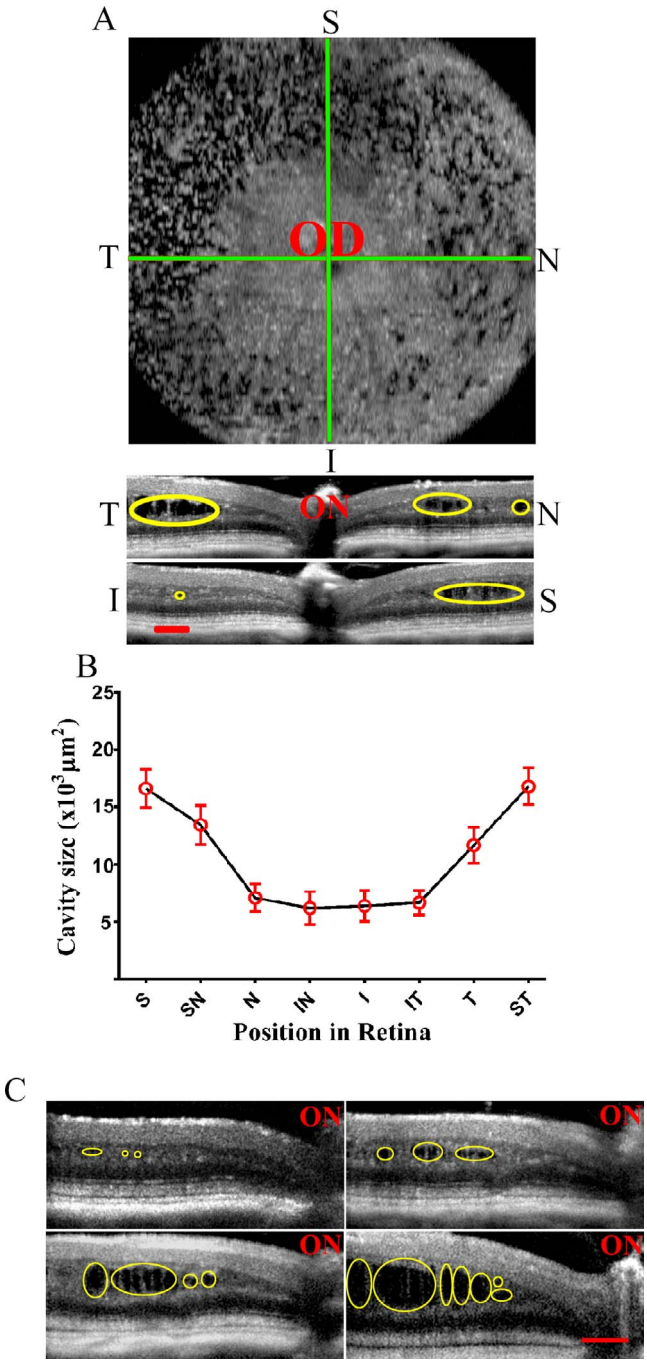

Figure 2. Uneven distribution of cavities and individual variation among *Rs1*-KO mouse retinas. (**A**) Representative OCT images from one animal: *top image* is the transverse view of a rectangular volume scan at the INL level; the dark areas are cavities; *bottom images* show two cross-sections centered on the optic nerve taken from the same retina with a radial volume scan, one in the temporal/nasal plane, and the other in the superior/inferior plane; these images show that there are larger and more frequent cavities (*yellow circle*) in the superior and temporal sides than in the inferior and nasal sides. (**B**) The spatial distribution of cavities in *Rs*1-KO mice at 4 months of age (±SD, $n = 23$/position). (**C**) Optical coherence tomography images from four *Rs1*-KO mice at the same age, showing wide individual variation in prevalence of cavities (*yellow circles*). I, inferior; IN, inferior nasal; IT, inferior temporal; N, nasal; OD, right eye; S, superior; SN, superior nasal; ST, superior temporal; T, temporal. *Scale bars*: 100 μm.

Table. Retinal Morphologic Features Revealed by OCT Imaging in *Rs1*-KO Mouse Over Time and Following AAV8-*RS1* Treatment

Phenotype	Untreated (Natural History), Age			Treated,
	1 mo	4 mo	12 mo	12–15 wk pi
Cavity size, $\times 10^3$ μm^2	2.52 ± 0.39	19.40 ± 2.02	0.17 ± 0.04	2.64 ± 0.80
ONL thickness, μm	39 ± 2	32 ± 2	25 ± 2	35 ± 3
OLM distortion	+	±	−	−
Second and third ORRBs merged	+	+	+	−

pi, post injection.

examples of OCT images taken in the same location from four separate *Rs1*-KO mice at 4 ½ months of age. At this age, the sum of the area of all cavities in each retinal image averaged 19,404 ± 2018 μm^2 (mean ± SD, $n = 38$) and ranged from 2328 to 54,948 μm^2. The ONL thickness was also variable, ranging from 26 to 36 μm and averaging 32 ± 2 μm ($n = 35$). In summary, these results demonstrated a wide variability in cavity formation, cavity distribution, and ONL thickness between and within individual animals.

Natural History of *Rs1*-KO Morphologic Phenotype

We monitored the natural history changes by using SD-OCT scans in approximately 200 *Rs1*-KO mice of five different ages. Figure 3A shows the OCT cross-sectional images from WT and *Rs1*-KO mice at 1, 2, 4, 8, and 12 months. The *Rs1*-KO images at 4 and 8 months were collected from the same mice. In WT mice, retinal laminar structure was maintained well through the entire period of the experiment; the four ORRBs remained distinct without any changes at all five time points (Fig. 3A, left), even though we did detect a mild but significant ($P < 0.0001$, $n = 68$) reduction in the ONL thickness with age (Fig. 3B, right). In *Rs1*-KO mice, cavity formation, indistinct INL and OPL margins, reduced ONL thickness, and alteration in the ORRB were seen to varying degrees depending on age (Fig. 3A, right). Cavities were observed as early as 3 weeks (data not shown), and showed a significant increase in size between 1 and 4 months ($P < 0.0001$, $n = 8$ and 38, respectively). Between 4 and 8 months there was a significant decline in cavity size ($P < 0.0001$, $n = 38$ and 19, respectively), after which no significant change occurred out to 12 months (Fig. 3B, left). The ONL thickness of *Rs1*-KO mice was 62% of WT by the end of the first postnatal month ($P < 0.0001$, $n = 8, 6$). It continued to decrease, but at a much slower pace, reaching 43% of WT ($P < 0.0001$, $n = 18$ and 11, respectively) at 12 months (Fig. 3B, right). The scatter plots in Figure 3B also indicate that there was substantial variation between animals of the same age. Figure 3C shows the changes in ORRB appearance over time. The ORRB1 was fragmented at 1 month, but by 8 months it was less so, and it had a normal appearance at 12 months of age. Outer retina reflective band 2 and ORRB3 merged into one wider band by 1 month and this remained through the entire period that we investigated. The Table summarizes the natural history changes of *Rs*1-KO mice.

Anatomic Correlates to OCT Outer Retina Reflective Bands

The region between the ONL and RPE resolves into four reflective bands in OCT images of WT mouse retina similar to the perifoveal region of human retina.[37,38] Based on these studies, the corresponding anatomic structures of these bands by position in histologic sections are as follows, from innermost to outermost: OLM (1), the boundary of the IS and OS or the ellipsoid portion of the IS (2), the distal portion of the OS (3), and the RPE (4), as depicted in Figure 4A. To confirm the correlation of these bands with retinal structures, retinal sections were immunolabeled with antibodies for OxPhos Complex IV (COX4) subunit I, a mitochondrial enzyme that can be used as a marker for the ellipsoid portion of the IS,[39] and β-catenin, a subunit of cadherin that can be used as a marker for the OLM.[40] COX4 labeling of mitochondria in the IS ellipsoid appeared as long, thin, and tightly packed parallel structures (Fig. 4B) that aligned well with ORRB2 in OCT images (Fig. 4A). The dark region between band 1 and band 2 lined up with the myoid portion of the IS that was not labeled by COX4 subunit I antibody and contained very few mitochondria. The H&E-stained section of WT retina confirmed the alignment of band 2 and COX4 labeling with the distal IS, though some shrinkage occurred during preparation of the plastic section (Fig. 4C).

The middle and lower panels of Figure 4 show the anatomic correlation between the β-catenin–labeled OLM and the first OCT ORRB in WT and *Rs1*-KO retinas at 1 month and 8 months. This figure demonstrates that both the β-catenin–labeled OLM in retina sections (Figs. 4D, 4F) and the OCT ORRB1 (Figs. 4E, 4G) in WT were evident as a well-defined line that did not change with age. In contrast, the OCT ORRB1 (Fig. 4I) and the β-catenin–labeled OLM (Fig. 4H) in *Rs1*-KO retinas appeared as a broken line at 1 month that returned back to normal at 8 months (Figs. 4J, 4K). In 1-month-old *Rs1*-KO retinas, photoreceptor cells located outside the ONL had penetrated the OLM, intruding into the space between inner segments, accounting for the gaps seen in the OLM revealed by immunohistochemistry and OCT.

Gene Therapy Outcome Assessment Using SD-OCT

The AAV-*RS1* vector was injected intravitreally into the eyes of *Rs1*-KO mice between the ages of 21 and 26 days. The evaluation time point for this study was 12 to 15 weeks post injection and was based on our earlier studies in these mice. At this time (4 months of age), the animal model displayed the maximum *Rs1*-KO phenotype without treatment. Figure 5A depicts examples of OCT scans collected from *Rs1*-KO mice without (left panel) and with (right panel) *RS1* gene transfer. As described above, the retinal images of untreated eyes showed large cavities splitting the OPL and INL and blurring the margin between these two layers. Outer retina reflective band 1 was indistinct and/or fragmented, ORRB2 and ORRB3 merged together to form a thicker middle band, and the thickness of the ONL was reduced significantly. In contrast, treated eyes showed much more organized retinal laminar structure: the size of cavities was reduced significantly ($P < 0.0001$; Fig. 5B) or was completely absent, the margin of OPL and INL became more distinct, ORRB1 had a normal appearance, ORRB2 was separate from ORRB3, and the ONL thickness was partially preserved ($P < 0.0001$; Fig. 5C). The Table summarizes these effects of AAV8-mediated *RS1* gene transfer on treated *Rs1*-KO retinas.

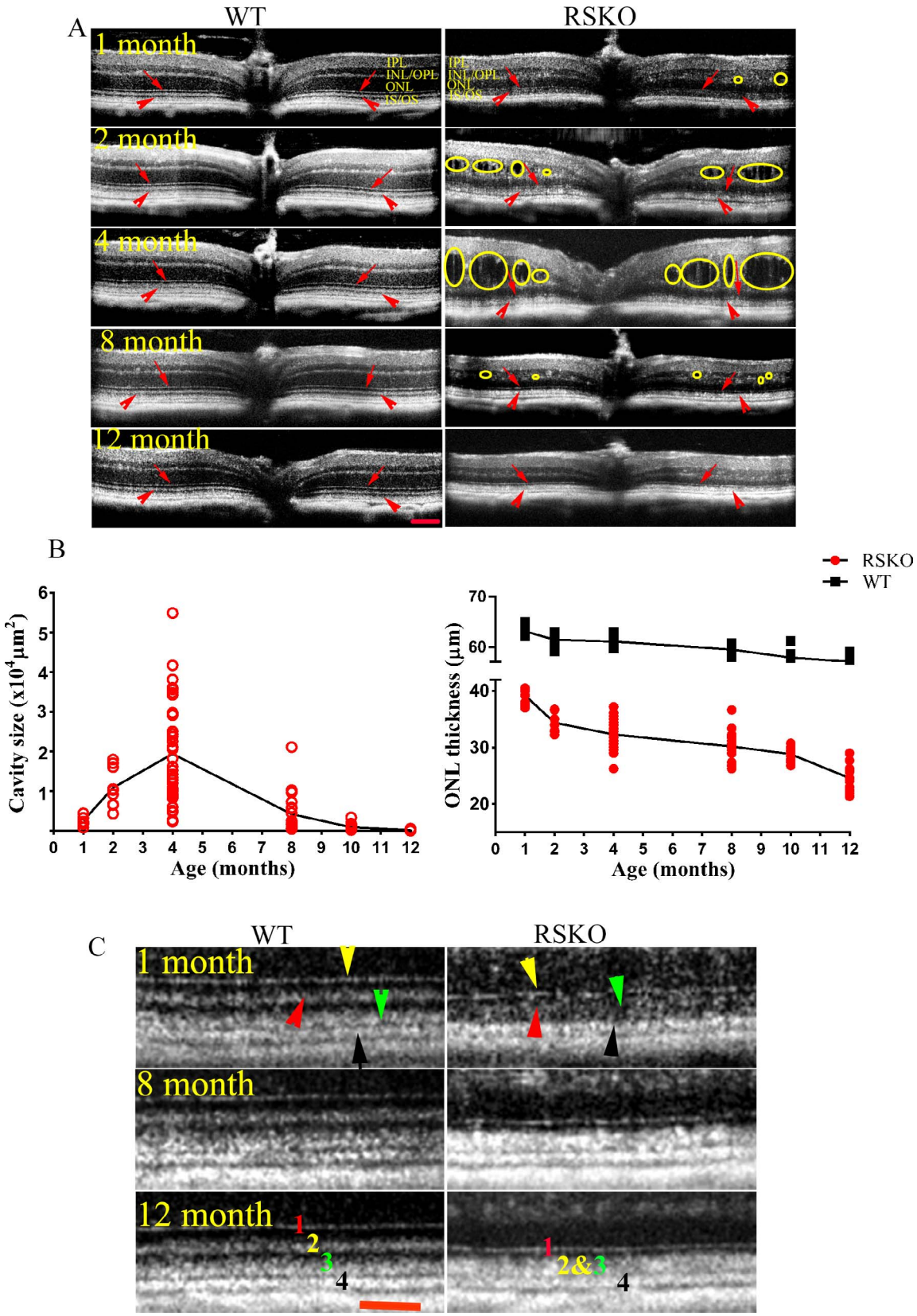

Figure 3. Natural history of retinal changes in the *Rs1*-KO mouse model. (**A**) Optical coherence tomography images collected from the WT and *Rs1*-KO mice at 1, 2, 4, 8, and 12 months of age. In *Rs1*-KO mice, very small cavities appear at 1 month of age (*small circle*); cavity formation is severe at 4 months (*large circle*), but they decrease markedly by 8 months and are almost gone at 12 months of age. Unlike WT, the innermost outer retina reflective band in *Rs1*-KO is indistinct and fragmented at 1 month of age, but returns to a normal appearance by 8 months (*red arrows*); the second outer retina reflective band merges with the third band during the entire course of the study (*arrowheads*). (**B**) Changes in the cavity size (*left*) and ONL thickness (*right*) in *Rs1*-KO mice. There is a substantial variation between animals at each age. (**C**) Changes in the OCT outer retina

Investigative Ophthalmology & Visual Science

reflective bands over time in *Rs1*-KO mice compared to WT. *Arrowheads* point to the outer retina reflective bands numbered from innermost to outermost: *yellow* (1), *red* (2), *green* (3), *black* (4). The four bands are clearly separated, and the first band is a continuous well-defined line at all ages in WT retinas. In *Rs1*-KO mice, the first band is fragmented and less distinct than in WT at 1 month, but becomes more distinct and less fragmented by 8 months, and returns back to a well-defined line at 12 months; the second and third outer bands merge together forming a thicker band starting at 1 month, which remains during the entire experimental period (12 months). *Scale bars*: 100 μm (**A**); 50 μm (**C**).

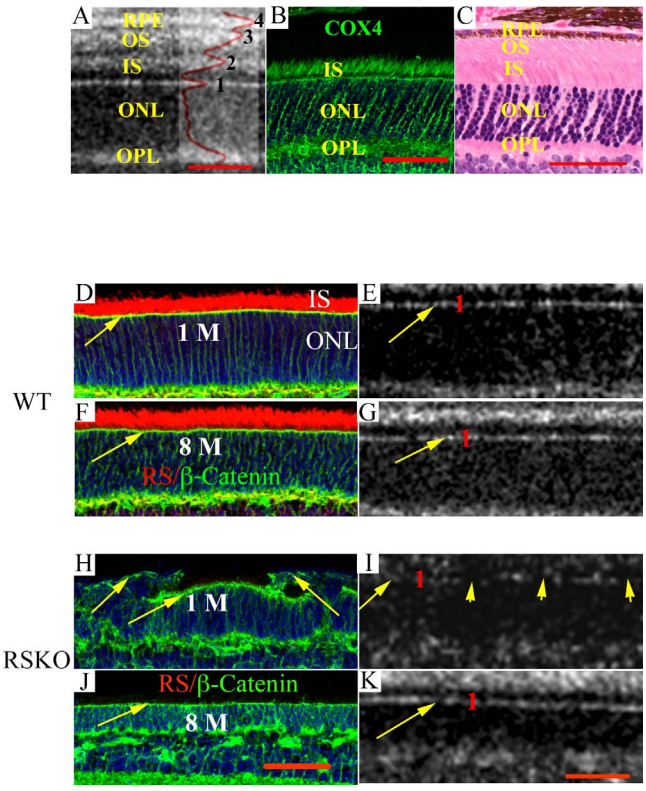

Figure 4. Anatomic correlates of OCT outer retina reflective bands. (**A**) Optical coherence tomography scan, (**B**) cryosection with immunolabeling, and (**C**) plastic section with H&E staining from a WT mouse. Outer retina reflective bands in (**A**) are numbered as in Figure 3, and the *peaks* of the intensity plot profile superimposed on the figure created with ImageJ indicate the position of the maximum brightness of each of these four bands. (**B**) COX4 subunit I labeling, a marker for mitochondria, which accounts for 75% of the volume of the IS ellipsoid, in WT retina. The second outer retina reflective band of the OCT image aligns with the COX4 labeling of the IS mitochondria, indicating that this band corresponds to the ellipsoid portion of the IS. For comparison of the position of COX4 labeling and OCT bands to conventional histology, (**C**) shows an H&E-stained plastic section. Although some shrinkage occurs during tissue preparation for plastic embedding, the RPE, OS, IS, ONL, and OPL line up relatively well with the OCT image (**A**) and COX4 subunit I–labeled cryosection (**B**). (**D**–**G**) Images of sections immunostained for β-catenin (**D**, **F**), or OCT scans (**E**, **G**) from WT mice at 1 or 8 months of age. *Yellow arrows* point to the OLM on both β-catenin–labeled and OCT images. The OLM in WT is a well-defined line at both ages. (**H**–**K**) Images from *Rs1*-KO retinas: (**H**, **J**) β-catenin–labeled retinas and (**I**, **K**) OCT images from 1-month-old and 8-month-old mice. The β-catenin–labeled OLM at 1 month (**H**), evident in the OCT image as a fragmented first outer retina reflective band (**I**, *yellow arrowheads* point to the broken area), is broken up by photoreceptor cells intruding into the space between IS; at 8 months of age the β-catenin–labeled OLM returns back to a well-defined line (**J**) consistent with the first outer retina reflective band of the OCT image (**K**). IPL, inner plexiform layer; INL, inner nuclear layer; OPL, outer plexiform layer; ONL, outer nuclear layer; IS, inner segment; OS, outer segment; RPE, retinal pigment epithelium. *Scale bar*: 50 mm.

Correlation of Improvement in the Second Outer Retina Reflective Band With IS Mitochondria Distribution Following AAV8-*RS1* Treatment

RS1 expresses heavily in the entire photoreceptor IS,[7,8,41,42] consistent with RS1 labeling in Figure 6A. As shown in Figure 4, top panel, and Figure 6D, COX4 labeling of the mitochondria in the IS ellipsoid aligns with ORRB2, while the unlabeled IS myoid lines up with the dark region between ORRB1 and ORRB2 (Figs. 4A, 6D), indicating that the first outer retinal dark band and ORRB2 in OCT images (Fig. 6G) correspond to the region of the IS in WT mouse. In the absence of RS1 in untreated *Rs1*-KO mice (Fig. 6B), the IS labeling by the COX4 subunit I was highly disorganized and lost the clear separation between the mitochondria-containing ellipsoid and the myoid (Fig. 6E). In OCT images, ORRB2 and ORRB3 merged into a single thicker band (Fig. 6H). After treatment, anti-RS1 showed intense IS labeling (Fig. 6C), and IS morphology in COX4 subunit I–labeled sections had a pattern identical to that of WT retinas (Fig. 6F). Corresponding to these changes, ORRB2 separated from ORRB3, restoring the outer retina bands back to near-normal appearance (Fig. 6I). Immunoelectron microscopy revealed IS mitochondrial morphology in WT and untreated and treated *Rs1*-KO retinas. In WT and treated retinas, anti-RS1 labeled the external IS plasma membrane, and mitochondria were adjacent to the internal plasma membrane and absent from the central cytoplasm (Figs. 6J, 6L). In contrast, no RS1 labeling on the external IS plasma membrane was detected in untreated *Rs1*-KO mice, and mitochondria occupied the entire IS space and were not limited to the periphery (Fig. 6K). Our results suggest that restoration of ORRB2 and ORRB3 configurations after AAV-mediated RS1 augmentation corresponds to a return of normal mitochondria distribution in the IS ellipsoid.

Discussion

We used the advantages of SD-OCT technology to collect virtual cross-sections of retina and characterize the disease phenotype of *Rs1*-KO mice, an experimental model of XLRS in humans. We found that the natural history of ONL thickness and inner retinal cavities and their spatial distribution were consistent with the results using traditional histologic approaches that have been previously reported.[7,13] We have previously shown that AAV-mediated gene transfer can result in RS1 protein expression in the *Rs1*-KO retina and restores retinal function while preserving morphology in the *Rs1*-KO mouse eye.[8,13,43] In those studies, we have used histologic methods to examine changes and improvements in retinal structure. Here we reported similar results for inner retinal cavities in vivo, using OCT images collected after gene delivery. These images showed that schisis cavities were reduced significantly or had disappeared entirely by 12 to 15 weeks post AAV-*RS1* injection. We also showed that the ONL thickness was preserved in treated eyes compared to the fellow untreated eyes. In addition, we described a new aspect of the *Rs1*-KO phenotype: changes in the ORRBs.

We identified consistent alterations in the ORRBs in *Rs1*-KO mice that correlated with anatomic changes observed by immunohistochemistry and EM and that responded to treat-

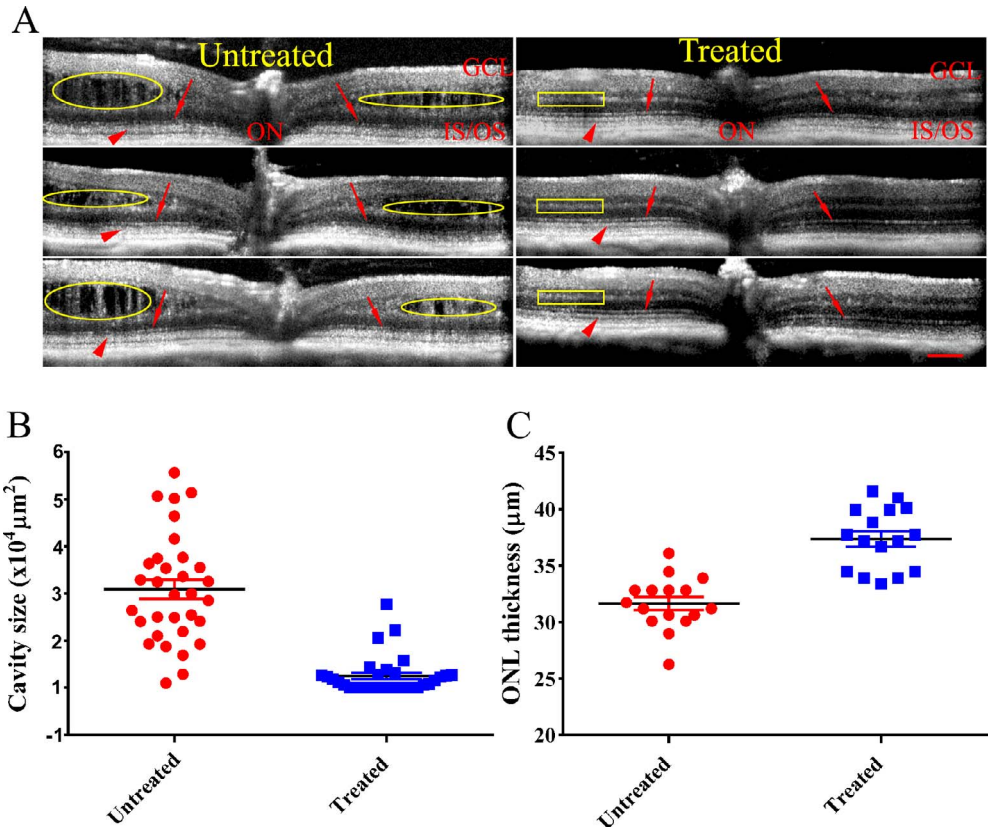

Figure 5. Evaluation of the treatment outcomes in *Rs1*-KO mice following AAV8-mediated RS1 gene transfer. (**A**) Optical coherence tomography images of *Rs1*-KO mouse retinas before (*left*) and after (*right*) AAV8-mediated gene replacement therapy. Treated retinas show much more organized retinal laminas: the margin of OPL and INL, OPL and ONL became more distinct (*yellow circle on left* displays untreated margin; *yellow rectangular box* shows treated margin), OLM becomes a defined line in treated retina (*small red arrows*); the second outer reflective band is separated from the third outer retina reflective band (*red arrowheads*). The number and size of cavities decrease, or cavities completely disappear. The OCT images of treated and untreated retinas were analyzed for cavity size (**B**) and ONL thickness (**C**). The size of cavities is reduced significantly ($P < 0.0001$), and the ONL thickness from treated retina is preserved ($P < 0.0001$) (**C**). Retinas were analyzed 4 months post unilateral intravitreal injection of AAV8-*RS1* at 3 weeks of age. Average ± SEM is plotted. *Scale bar*: 100 µm.

ment with AAV-mediated gene delivery. Outer retina reflective band 1, which is not normally visible in conventionally stained histologic sections, has been identified as the OLM, consisting of Müller cell junctions with photoreceptors, based on the known position of this structure.[22,44] These junctional complexes contain the cell adhesion protein β-catenin, and we confirmed the identity of ORRB1 as the OLM by its alignment with a β-catenin–stained structure in WT mouse and similar changes with age and treatment in *Rs1*-KO mouse: ORRB1 was indistinct and fragmented in young *Rs1*-KO mice at a time when many photoreceptor cells had penetrated the β-catenin–labeled OLM and intruded into the subretinal space; the fragmented ORRB1 became normal or near normal in appearance by the age of 8 months when most, if not all, intruding photoreceptors were absent from the subretinal space, presumably due to cell death, and β-catenin labeling confirmed that the OLM was mostly intact. In addition, both ORRB1 and β-catenin labeling of the OLM returned to near-normal or normal appearance after AAV-*RS1* treatment. It is unknown whether movement of photoreceptors out of the ONL is the cause of breaks in the OLM or whether it becomes fragmented for some other reason. As RS1 protein does not colocalize with Müller cells in mouse[41,42] or human,[41] and expression of *Rs1* RNA has not been detected in mouse Müller cells,[42] a direct effect of RS1 depletion on the Müller cell end-feet in the *Rs1*-KO is not expected.

Outer retina reflective band 2 and 3 also were altered in the *Rs1*-KO mouse retina but did not show an age-related progression. These bands align with the ellipsoid portion of the IS of rods and cones in the human perifovea (−1.5 to 1.5 mm eccentricity),[37,38] in which approximately 90% of the photoreceptors are rods[45] compared to 97% rods in the mouse retina.[46] We confirmed the alignment of ORRB2 with the IS ellipsoid in WT mice by labeling with an antibody against the mitochondrial enzyme COX4 subunit I, since mitochondria account for 75% of the ellipsoid volume. It has been shown, however, using adaptive optics OCT[47,48] and Gaussian-based modeling of raw OCT data,[37] that ORRB2 is actually localized to the outer ⅓ of the ellipsoid. In the contrast-enhanced images normally used for viewing, as in the present study, the hyperreflective bands are wider than the underlying source structures.[37]

COX4-labeled ISs were tightly packed parallel structures in WT retinas, but were highly disorganized in *Rs1*-KO retinas. Electron microscopy revealed that the IS of *Rs1*-KO mice lacked the regular array of densely packed, long thin mitochondria adjacent to the internal plasma membrane seen in WT. Instead, they were present throughout the cytoplasm. In *Rs1*-KO mice, ORRB2 and ORRB3 merged together and formed a single thicker band, essentially missing the intervening darker band between these two bright bands. Inner segment mitochondria were restored to a more normal appearance after *RS1* gene therapy, and ORRB2 and ORRB3

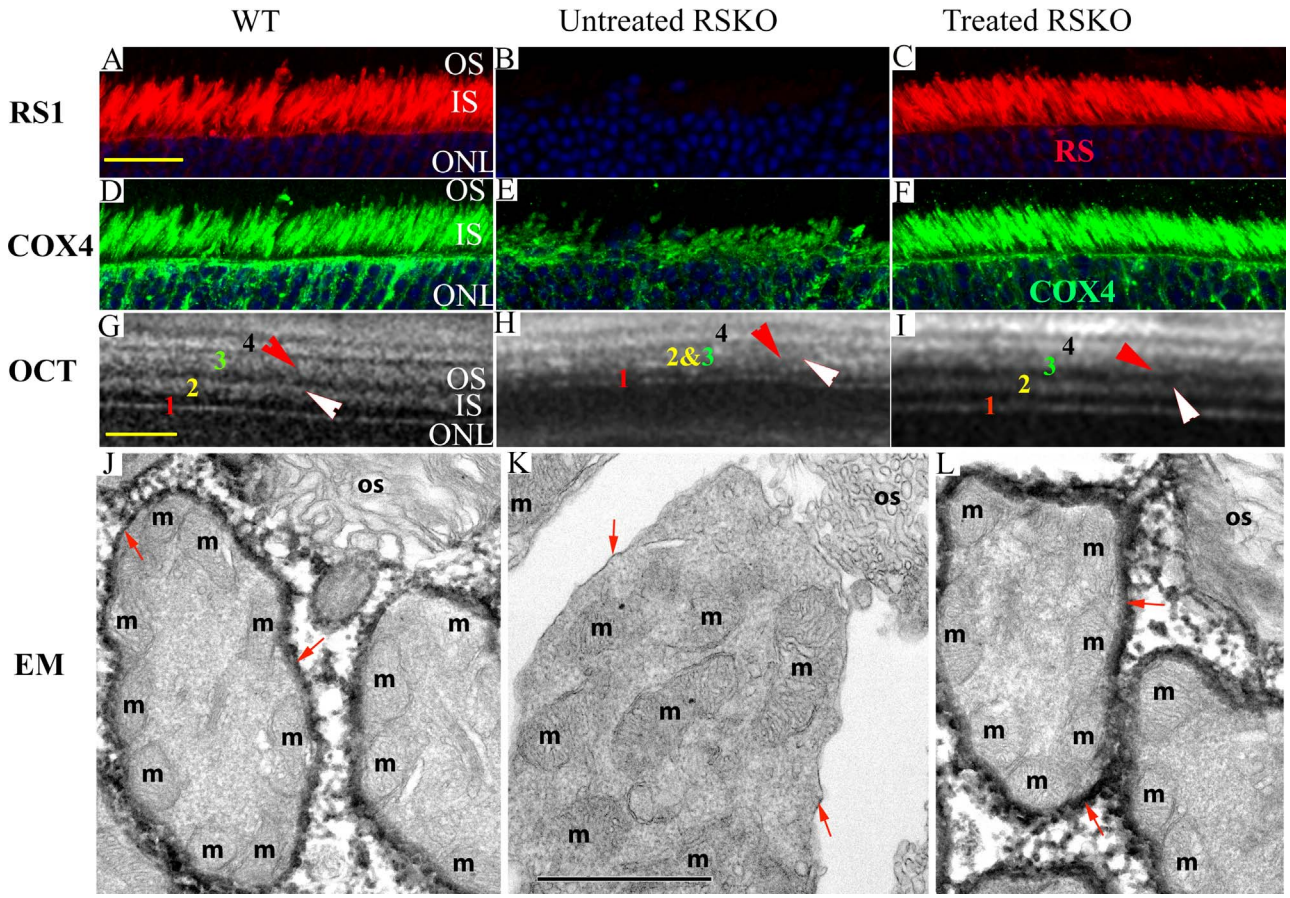

Figure 6. Improvement in the second outer retina reflective band and change in IS mitochondria distribution following AAV-*RS1* treatment. Strong RS expression is evident in both WT (**A**) and treated *Rs1*-KO retinas (**C**), but is absent in untreated *Rs1*-KO retinas (**B**). COX4 staining of mitochondria in WT (**D**) and treated *Rs1*-KO (**F**) mice shows that IS ellipsoids are packed tightly in parallel, but become highly disorganized in *Rs1*-KO mice (**E**). In OCT images from WT (**G**), untreated *Rs1*-KO (**H**), and treated *Rs1*-KO mice (**I**), a *white arrowhead* points to the second outer retina band, and a *red arrowhead* points to the third outer retina band. In the WT and treated *Rs1*-KO retinas, these two bands are distinctly separate (**G**, **I**, respectively) but merge together in untreated *Rs1*-KO retinas (**H**). In immunoelectron microscope images (**J**–**L**), WT (**J**) and treated *Rs1*-KO mice (**L**) mitochondria (m) are adjacent to the internal plasma membrane, and absent from the central cytoplasm, but they fill the entire IS in the untreated *Rs1*-KO retina (**K**). The *red arrows* point to the plasma membrane of the IS, which is densely labeled in WT and treated *Rs1*-KO retinas with RS1 antibody but shows no RS1 labeling in untreated *Rs1*-KO retinas. *Scale bars*: 50 μm for the OCT images and light microscope images; 1 μm for EM images.

returned to the WT configuration. This does not necessarily mean there is a direct link between the change in mitochondrial distribution in *Rs1*-KO retinas and loss of the dark band between reflective bands 2 and 3. However, a direct effect of mitochondria on OCT band reflectance could be due to a change in mitochondrial waveguide properties[39] resulting from their distribution in the IS, but it could also be due to disruption of IS morphology. Since the change in OCT ORRB2 and ORRB3 persists in *Rs1*-KO mouse at all ages, even when cavities are minimal and the OLM and laminar structure of the retina are more normal at later ages, perhaps RS1 on the IS plasma membrane plays a direct role in ORRB morphology. Whatever the cause, the merger of band 2 and 3 is a useful tool for evaluating the response to treatment in the *Rs1*-KO mouse. Yang et al.[49] report in their clinical studies that changes in the ORRBs may be closely associated with visual acuity in XLRS patients. Hence, the changes of these bands might be a useful indicator while monitoring outcomes of gene therapy in humans.

This study demonstrated that the new generation of SD-OCT is capable of identifying structural changes in the retina of the mouse model of XLRS, providing a detailed image of retinal laminar structures that allows monitoring disease progression and treatment response. The quality of OCT images allowed tracking of a broad range of changes in retinal morphology in WT and *Rs1*-KO mice with results similar to our previous histologic studies of the natural history and effects of gene replacement treatment in *Rs1*-KO mice.[13] However, there are drawbacks in using OCT imaging. Optical coherence tomography is an interferometric technique that captures reflected light from optical scattering media to produce an image[20] and requires transparent ocular media. Opacity of any of these tissues will interfere with the light path and image quality. Quantitative measurement using OCT is not completely free from artifacts, as the optical properties might vary between layers of different lipid composition, and logarithmic filtering, which is frequently applied to SD-OCT data, can change the apparent thickness of different layers.[37,50] In spite of these disadvantages, there are considerable benefits for using OCT to image retinal structure, as it eliminates tissue processing, enables doing longitudinal studies, and reduces the number of animals needed. Moreover, as our findings on the ORRBs demonstrated, it may provide new noninvasive and sensitive indicators to monitor the overall health and functionality of the human retina.

Investigative Ophthalmology & Visual Science

Acknowledgments

The authors thank Maria Santos and Jinbo Li for technical assistance, and Haohua Qian and Lisa Wei for reviewing the manuscript.

Supported by the Intramural Research Program of the National Institutes of Health, National Institute on Deafness and other Communication Disorders (ZIC, DC000065-14, DC000081-03), and the National Eye Institute.

Disclosure: **Y. Zeng**, None; **R.S. Petralia**, None; **C. Vijayasarathy**, None; **Z. Wu**, None; **S. Hiriyanna**, None; **H. Song**, None; **Y.-X. Wang**, None; **P.A. Sieving**, None; **R.A. Bush**, None

References

1. Forsius H, Vainio-Mattila B, Eriksson A. X-linked hereditary retinoschisis. *Br J Ophthalmol*. 1962;46:678–681.
2. George ND, Yates JR, Moore AT. X linked retinoschisis. *Br J Ophthalmol*. 1995;79:697–702.
3. Mooy CM, Van Den Born LI, Baarsma S, et al. Hereditary X-linked juvenile retinoschisis: a review of the role of Müller cells. *Arch Ophthalmol*. 2002;120:979–984.
4. Azzolini C, Pierro L, Codenotti M, Brancato R. OCT images and surgery of juvenile macular retinoschisis. *Eur J Ophthalmol*. 1997;7:196–200.
5. Molday RS, Kellner U, Weber BH. X-linked juvenile retinoschisis: clinical diagnosis, genetic analysis, and molecular mechanisms. *Prog Retin Eye Res*. 2012;31:195–212.
6. Molday LL, Min SH, Seeliger MW, et al. Disease mechanisms and gene therapy in a mouse model for X-linked retinoschisis. *Adv Exp Med Biol*. 2006;572:283–289.
7. Weber BH, Schrewe H, Molday LL, et al. Inactivation of the murine X-linked juvenile retinoschisis gene, Rs1h, suggests a role of retinoschisin in retinal cell layer organization and synaptic structure. *Proc Natl Acad Sci U S A*. 2002;99:6222–6227.
8. Zeng Y, Takada Y, Kjellstrom S, et al. RS-1 gene delivery to an adult Rs1h knockout mouse model restores ERG b-wave with reversal of the electronegative waveform of X-linked retinoschisis. *Invest Ophthalmol Vis Sci*. 2004;45:3279–3285.
9. Byrne LC, Ozturk BE, Lee T, et al. Retinoschisin gene therapy in photoreceptors, Müller glia or all retinal cells in the Rs1h-/- mouse. *Gene Ther*. 2014;21:585–592.
10. Veazey RS. Animal models for microbicide safety and efficacy testing. *Curr Opin HIV AIDS*. 2013;8:295–303.
11. Acland GM, Aguirre GD, Ray J, et al. Gene therapy restores vision in a canine model of childhood blindness. *Nat Genet*. 2001;28:92–95.
12. Koenekoop RK. An overview of Leber congenital amaurosis: a model to understand human retinal development. *Surv Ophthalmol*. 2004;49:379–398.
13. Kjellstrom S, Bush RA, Zeng Y, Takada Y, Sieving PA. Retinoschisin gene therapy and natural history in the Rs1h-KO mouse: long-term rescue from retinal degeneration. *Invest Ophthalmol Vis Sci*. 2007;48:3837–3845.
14. Min SH, Molday LL, Seeliger MW, et al. Prolonged recovery of retinal structure/function after gene therapy in an Rs1h-deficient mouse model of x-linked juvenile retinoschisis. *Mol Ther*. 2005;12:644–651.
15. Janssen A, Min SH, Molday LL, et al. Effect of late-stage therapy on disease progression in AAV-mediated rescue of photoreceptor cells in the retinoschisin-deficient mouse. *Mol Ther*. 2008;16:1010–1017.
16. Day TP, Byrne LC, Schaffer DV, Flannery JG. Advances in AAV vector development for gene therapy in the retina. *Adv Exp Med Biol*. 2014;801:687–693.
17. Huber G, Beck SC, Grimm C, et al. Spectral domain optical coherence tomography in mouse models of retinal degeneration. *Invest Ophthalmol Vis Sci*. 2009;50:5888–5895.
18. Xu J, Molday LL, Molday RS, Sarunic MV. In vivo imaging of the mouse model of X-linked juvenile retinoschisis with fourier domain optical coherence tomography. *Invest Ophthalmol Vis Sci*. 2009;50:2989–2993.
19. Fischer MD, Huber G, Beck SC, et al. Noninvasive, in vivo assessment of mouse retinal structure using optical coherence tomography. *PLoS One*. 2009;4:e7507.
20. Huang D, Swanson EA, Lin CP, et al. Optical coherence tomography. *Science*. 1991;254:1178–1181.
21. Li Q, Timmers AM, Hunter K, et al. Noninvasive imaging by optical coherence tomography to monitor retinal degeneration in the mouse. *Invest Ophthalmol Vis Sci*. 2001;42:2981–2989.
22. Ruggeri M, Wehbe H, Jiao S, et al. In vivo three-dimensional high-resolution imaging of rodent retina with spectral-domain optical coherence tomography. *Invest Ophthalmol Vis Sci*. 2007;48:1808–1814.
23. Kim KH, Puoris'haag M, Maguluri GN, et al. Monitoring mouse retinal degeneration with high-resolution spectral-domain optical coherence tomography. *J Vis*. 2008;8(1):17.
24. Zhour A, Bolz S, Grimm C, et al. In vivo imaging reveals novel aspects of retinal disease progression in Rs1h(-/Y) mice but no therapeutic effect of carbonic anhydrase inhibition. *Vet Ophthalmol*. 2012;15(suppl 2):123–133.
25. Ohno Y, Makita S, Shimazawa M, Tsuruma K, Yasuno Y, Hara H. Thickness mapping of the inner retina by spectral-domain optical coherence tomography in an N-methyl-D-aspartate-induced retinal damage model. *Exp Eye Res*. 2013;113:19–25.
26. Lesch B, Szabo V, Kanya M, et al. Truncation of retinoschisin protein associated with a novel splice site mutation in the RS1 gene. *Mol Vis*. 2008;14:1549–1558.
27. Laliberte AM, MacPherson TC, Micks T, Yan A, Hill KA. Vision deficits precede structural losses in a mouse model of mitochondrial dysfunction and progressive retinal degeneration. *Exp Eye Res*. 2011;93:833–841.
28. Seo S, Mullins RF, Dumitrescu AV, et al. Subretinal gene therapy of mice with Bardet-Biedl syndrome type 1. *Invest Ophthalmol Vis Sci*. 2013;54:6118–6132.
29. Aziz MK, Ni A, Esserman DA, Chavala SH. Evidence of early ultrastructural photoreceptor abnormalities in light-induced retinal degeneration using spectral domain optical coherence tomography. *Br J Ophthalmol*. 2014;98:984–989.
30. Boye SE, Huang WC, Roman AJ, et al. Natural history of cone disease in the murine model of Leber congenital amaurosis due to CEP290 mutation: determining the timing and expectation of therapy. *PLoS One*. 2014;9:e92928.
31. Neuille M, El Shamieh S, Orhan E, et al. Lrit3 deficient mouse (nob6): a novel model of complete congenital stationary night blindness (cCSNB). *PLoS One*. 2014;9:e90342.
32. Marangoni D, Wu Z, Wiley HE, et al. Preclinical safety evaluation of a recombinant AAV8 vector for X-linked retinoschisis after intravitreal administration in rabbits. *Hum Gene Ther Clin Dev*. 2014;25:202–211.
33. Wilkins GR, Houghton OM, Oldenburg AL. Automated segmentation of intraretinal cystoid fluid in optical coherence tomography. *IEEE Trans Biomed Eng*. 2012;59:1109–1114.
34. Pilch M, Stieger K, Wenner Y, et al. Automated segmentation of pathological cavities in optical coherence tomography scans. *Invest Ophthalmol Vis Sci*. 2013;54:4385–4393.
35. Petralia RS, Wenthold RJ. Immunocytochemistry of NMDA receptors. *Methods Mol Biol*. 1999;128:73–92.
36. Petralia RS, Wang YX, Hua F, et al. Organization of NMDA receptors at extrasynaptic locations. *Neuroscience*. 2010;167:68–87.

37. Ross DH, Clark ME, Godara P, et al. RefMoB, a reflectivity feature model-based automated method for measuring four outer retinal hyperreflective bands in optical coherence tomography. *Invest Ophthalmol Vis Sci*. 2015;56:4166–4176.
38. Spaide RF, Curcio CA. Anatomical correlates to the bands seen in the outer retina by optical coherence tomography: literature review and model. *Retina*. 2011;31:1609–1619.
39. Hoang QV, Linsenmeier RA, Chung CK, Curcio CA. Photoreceptor inner segments in monkey and human retina: mitochondrial density, optics, and regional variation. *Vis Neurosci*. 2002;19:395–407.
40. Song H, Bush RA, Vijayasarathy C, Fariss RN, Kjellstrom S, Sieving PA. Transgenic expression of constitutively active RAC1 disrupts mouse rod morphogenesis. *Invest Ophthalmol Vis Sci*. 2014;55:2659–2668.
41. Molday LL, Hicks D, Sauer CG, Weber BH, Molday RS. Expression of X-linked retinoschisis protein RS1 in photoreceptor and bipolar cells. *Invest Ophthalmol Vis Sci*. 2001;42:816–825.
42. Takada Y, Fariss RN, Tanikawa A, et al. A retinal neuronal developmental wave of retinoschisin expression begins in ganglion cells during layer formation. *Invest Ophthalmol Vis Sci*. 2004;45:3302–3312.
43. Park TK, Wu Z, Kjellstrom S, et al. Intravitreal delivery of AAV8 retinoschisin results in cell type-specific gene expression and retinal rescue in the Rs1-KO mouse. *Gene Ther*. 2009;16:916–926.
44. Bernstein MH. The interphotoreceptor matrix and the interphotoreceptor space of the vertebrate retina. *Scan Electron Microsc*. 1985;859–868.
45. Curcio CA, Allen KA, Sloan KR, et al. Distribution and morphology of human cone photoreceptors stained with anti-blue opsin. *J Comp Neurol*. 1991;312:610–624.
46. Jeon CJ, Strettoi E, Masland RH. The major cell populations of the mouse retina. *J Neurosci*. 1998;18:8936–8946.
47. Kocaoglu OP, Ferguson RD, Jonnal RS, et al. Adaptive optics optical coherence tomography with dynamic retinal tracking. *Biomed Opt Express*. 2014;5:2262–2284.
48. Meadway A, Girkin CA, Zhang Y. A dual-modal retinal imaging system with adaptive optics. *Opt Express*. 2013;21:29792–29807.
49. Yang HS, Lee JB, Yoon YH, Lee JY. Correlation between spectral-domain OCT findings and visual acuity in X-linked retinoschisis. *Invest Ophthalmol Vis Sci*. 2014;55:3029–3036.
50. Pennesi ME, Michaels KV, Magee SS, et al. Long-term characterization of retinal degeneration in rd1 and rd10 mice using spectral domain optical coherence tomography. *Invest Ophthalmol Vis Sci*. 2012;53:4644–4656.

Investigative Ophthalmology & Visual Science